

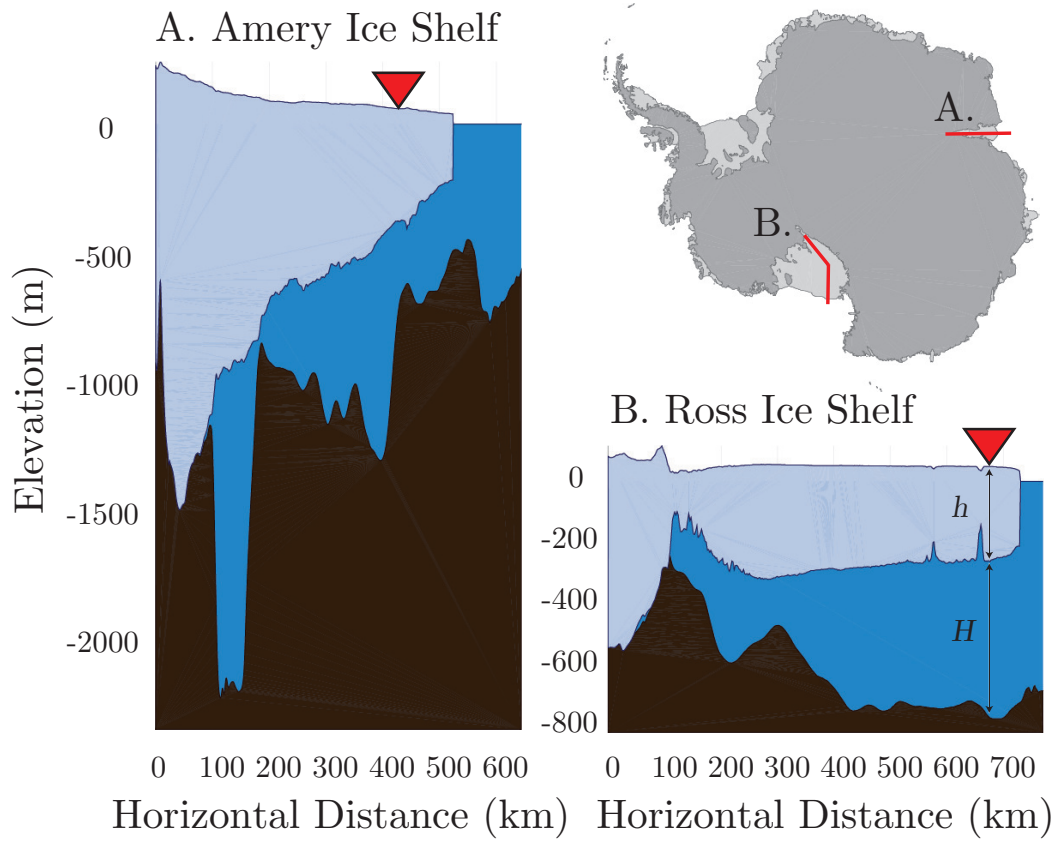
Abstract

Distant storms, tsunamis, and earthquakes generate waves on floating ice shelves. Previous studies, however, have disagreed about whether the resulting wave-induced stresses may cause ice shelf rift propagation. Most ice shelf rifts show long periods of dormancy suggesting that they have low background stress concentrations and may therefore be susceptible to wave-induced stresses. Here, I quantify wave-induced stresses on the Ross Ice Shelf Nascent Rift and the Amery Ice Shelf Loose Tooth T2 Rift using passive seismology. I then relate these stresses to a fracture mechanical model of rift propagation that accounts for rift cohesive strength due to refrozen melange, ice inertia, and spatial heterogeneity in fracture toughness due to the presence of high toughness suture zones. I infer wave-induced stresses using the wave impedance tensor, a rank three tensor that relates seismically observable particle velocities to components of the stress tensor. I find that wave-induced stresses are an order of magnitude larger on the Ross Ice Shelf as compared to the Amery Ice Shelf. In the absence of additional rift strength, my model predicts that the Nascent Rift should have experienced extensive rift propagation. The observation that no such propagation occurred during this time therefore suggests that the Nascent Rift experiences strengthening from either refrozen melange or rift tip processes zone dynamics. This study illustrates one way in which passive seismology may illuminate glacier calving physics.

1 Introduction

Floating ice shelves exert a net buttressing force on grounded ice and therefore support the stability of ice sheets [Doake *et al.*, 1998; Rignot *et al.*, 2004; Scambos *et al.*, 2004]. The extent of ice shelves is often limited by the formation of 10 to 100 km long, through-thickness fractures called rifts. Rifts tend to grow in length until they connect to the ice front and create a tabular iceberg [Robin, 1979; Shabtaie and Bentley, 1982; Jacobs *et al.*, 1986; Keys *et al.*, 1998]. Observations show that rifts experience most of their growth during episodic bursts of activity [Joughin and MacAyeal, 2005] that last from seconds [Powell, 2015; Banwell *et al.*, 2017] to hours [Bassis *et al.*, 2005]. These short time scales suggest that rift propagation is a brittle process, meaning that during episodes of rift propagation the ice shelf is well-approximated as an elastic solid everywhere except in a small region near the rift tip [Broek, 2012]. Ductile fracture, in contrast, may occur by the slow coalescence of microcracks [Rice and Tracey, 1969; Lemaitre, 1985; Weiss, 2004; Pralong and Funk, 2005; Borstad *et al.*, 2012, 2013; Duddu and Waisman, 2013; Duddu *et al.*, 2013] and results in an essentially viscous-plastic ice rheology. Field observations show that ductile fracture also occurs in ice shelf rifts, although it typically is associated with slower growth [Bassis *et al.*, 2007]. Linear elastic fracture mechanics is well suited to describe brittle fracture and has previously been used in the study of ice shelf rift propagation, crevasse growth, calving, and hydrofracture [Weertman, 1971, 1973; Smith, 1976; Nemat-Nasser *et al.*, 1979; Van der Veen, 1998; Rist *et al.*, 2002; Larour *et al.*, 2004a; Alley *et al.*, 2005; Krawczynski *et al.*, 2009; Scambos *et al.*, 2009a; Plate *et al.*, 2012; Krug *et al.*, 2014; Yu *et al.*, 2017].

Brittle fracture is driven by loading applied to sharp geometrical features such as the tip of an ice shelf rift [Griffith, 1921]. The resulting stress concentration may be quantified using the stress intensity factor K [Irwin, 1957]. The stress intensity factor K may in turn be expressed entirely in terms of the loading exerted on a system [Rice, 1968], which in ice shelves consists of contributions from gravity, buoyancy, and interaction with grounded and floating ice [Weertman, 1957; Reeh, 1968]. Catalogs of Antarctic ice shelf rifts, however, show that this loading often results in zero measurable propagation over years to decades of observation [Walker *et al.*, 2013, 2015]. Rift propagation, when it does occur, is typically observed to be highly episodic in time [Bassis *et al.*, 2005]. In the context of linear elastic fracture mechanics, this observation suggests that ice shelf rifts commonly attain a state of stress such that $K < K_c$ and no propagation occurs. I argue that



52 **Figure 1.** Profiles showing the geometry of the Amery (A.) and Ross (B.) Ice Shelves and their position
 53 within the Antarctic Ice Sheet. The red triangles mark the locations of the two seismometers used in this
 54 study. The two cross sections are drawn at the same scale to emphasize geometrical differences between the
 55 two ice shelves.

67 this is the precise setting that allows ocean waves to effectively drive episodic ice shelf rift
68 propagation.

69 The exact mechanism responsible for the episodic nature of ice shelf rift propagation
70 remains the subject of multiple competing hypotheses in the literature. Three processes
71 have been proposed as being of importance: spatial heterogeneity of fracture toughness,
72 constitutive instability, and temporal variation in loading due to interaction with ocean
73 waves. In regards to spatial heterogeneity, ice shelf suture zones that form at provenance
74 boundaries in the ice shelf appear to be particularly important. Rapid rift tip propagation
75 events are often observed to terminate when the rift tip reaches an ice shelf suture zone
76 [Hulbe *et al.*, 2010; McGrath *et al.*, 2014; Borstad *et al.*, 2017]. Wave action also appears
77 to play a role. In studies of the Nascent Rift, MacAyeal *et al.* [2006] and Cathles *et al.*
78 [2009] revived the idea of Holdsworth and Glynn [1978] that wave-induced stresses might
79 cause rift propagation. However, Bassis *et al.* [2005, 2007, 2008] also analyzed *in situ*
80 seismic data from the Loose Tooth and concluded that rift propagation there was driven
81 primarily by glacial stresses. Although other studies have appeared to confirm the impor-
82 tance of wave action in rift propagation, these studies were limited by not having *in situ*
83 seismic data. Using remotely sensed imagery, Brunt *et al.* [2011] observed rift propaga-
84 tion following the arrival of a tsunami. Banwell *et al.* [2017] used a nearby seismometer
85 located on bedrock to show that a rift propagation event on the McMurdo Ice Shelf oc-
86 curred during the arrival of large amplitude ocean waves from a distant storm. Finally, a
87 constitutive instability, essentially the opening-mode equivalent of the shearing-mode stick-
88 slip instability [Lipovsky and Dunham, 2016, 2017], has been proposed to be important for
89 episodic rift motion [Larour *et al.*, 2004a]. One of the goals of this paper is to develop a
90 theoretical framework within which to compare the predictions of these hypotheses.

91 Seismometers located directly on floating ice shelves quantify the ice shelf wave
92 field. Using an appropriately defined transfer function called the wave impedance it is
93 therefore possible to calculate stresses from *in situ* velocity seismograms. In a similar
94 vein, Williams and Robinson [1981] used a transfer function approach to estimate water
95 pressure fluctuations from 1 min period gravimeter measurements on the Ross Ice Shelf.
96 The stresses carried by waves in ice shelves have been previously analyzed in an idealized
97 geometry by Holdsworth and Glynn [1978] and Sergienko [2010, 2013] and in more realis-
98 tic geometries by Konovalov [2014] and Sergienko [2017]. Each of these studies, however,
99 calculated the ice shelf response to idealized, monochromatic wave forcing. Here, I build
100 on these previous studies by estimating the stresses associated with the *in situ* ice shelf
101 wave fields as recorded by seismometers located on floating ice shelves. I begin this paper
102 in the first section by describing ice shelf wave impedances (Section 2).

103 I describe a fracture mechanical model of ice shelf rift propagation in Section 3. I
104 then apply this model to the wave-induced stresses inferred at sites near the Ross Ice Shelf
105 Nascent Rift and the Amery Ice Shelf Loose Tooth Rift (Sections 4 and 5). The principal
106 finding of this analysis is that, in the absence of some additional source of rift strength,
107 wave-induced stresses are predicted to have been sufficiently large to cause rift propaga-
108 tion on the Nascent Rift. Satellite imagery, however, shows that no observable rift propa-
109 gation occurred during the observation periods under consideration. This finding there-
110 fore suggests that the Nascent Rift experienced strengthening that prevented rift propaga-
111 tion during this time. One potential source of this strength is refreezing in the rift-filling
112 melange [MacAyeal *et al.*, 1998; Rignot and MacAyeal, 1998; Larour *et al.*, 2004b; Fricker
113 *et al.*, 2005]. This and other topics are discussed in Section 6.

114 The analysis presented here connects qualitative predictions of ice shelf instability
115 [Holdsworth and Glynn, 1978] to geophysical measurement [MacAyeal *et al.*, 2006; Bassis
116 *et al.*, 2007; Cathles *et al.*, 2009; Brunt *et al.*, 2011; Bromirski *et al.*, 2017] and therefore
117 unleashes the power of seismology to elucidate the detailed mechanics of ice shelf rift
118 propagation.

Shear modulus	μ	3.5 GPa
Young's modulus	E	9.3 GPa
Poisson ratio	ν	0.33
Density of ice	ρ	916 kg/m ³
Density of seawater	ρ_w	1024 kg/m ³
Dilatational wave speed	c_p	3750 m/s
Shear wave speed	c_s	1950 m/s
Fracture toughness	K_C	100 to 400 kPa $\sqrt{\text{m}}$

Table 1. Table of ice mechanical properties [Schulson *et al.*, 2009].

2 Wave stresses

Seismometers located directly on floating ice shelves measure the Lagrangian particle velocity, within a certain frequency range, of the parcel of ice on which they rest. In this section, I derive a transfer function called the wave impedance that relates these particle velocity perturbations to their associated stresses perturbations. I calculate wave impedances for two types of long period ice shelf waves: flexural waves and extensional waves. I will show that there are two main differences between these wave types. First, the flexural wave impedance is frequency-dependent but the extensional wave impedance is not. Second, flexural wave impedances tend to be much higher than extensional wave impedances. These results are summarized in Figures 2 and 3.

In order to write down expressions for the wave impedances, it is first necessary to describe the waves themselves. In Appendix A, I describe ice shelf wave motion in a finite-thickness elastic ice shelf over an inviscid, incompressible, finite-thickness water layer and rigid ocean floor. I consider waves that propagate in the direction of flow, and I treat a two dimensional cross section in the vertical and flow directions. Several limitations associated with these assumptions are discussed in Section 6. In Appendix B I show that waves with wavelength greater than the ice thickness may propagate as either flexural or extensional waves. I begin this section by describing the general wave impedance transfer function (Section 2.1).

2.1 Ice shelf wave impedances

The transfer function between the perturbation velocity vector component $v_l \equiv \partial u_l / \partial t$ and the perturbation stress tensor component σ_{ij} is called the wave impedance. It is defined as

$$Z_{ijl}(k, \omega) = \frac{\Sigma_{ij}(k, \omega)}{(-i\omega)U_l(k, \omega)}. \quad (1)$$

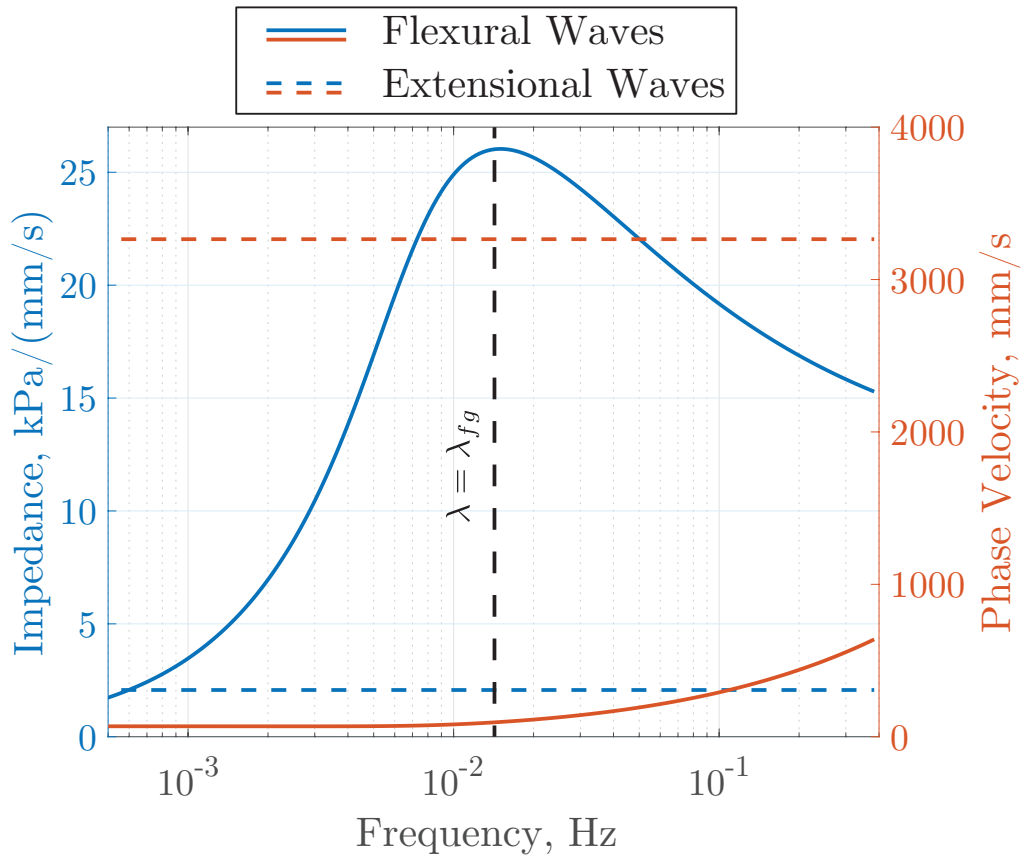
Here, the subscripts i , j , and l may vary over the three spatial coordinates x , y , and z . The spatial coordinates are defined so that x is in the direction of ice flow, z is positive upwards, and y is perpendicular to x and z following the right-hand-rule. Upper case letters denote the double Fourier transform in time t and in the horizontal direction x . For an arbitrary, adequately smooth function f , the Fourier transform of f is denoted,

$$F(k, z, \omega) = \int_{-\infty}^{\infty} \int_{-\infty}^{\infty} f(x, z, t) e^{i(kx - \omega t)} dx dt \quad (2)$$

This definition introduces the horizontal wavenumber k and frequency ω .

The impedance tensor defined in this way allows the estimation of wave field stresses using multiplication in the Fourier domain,

$$\sigma_{ij}(x, t) = \int_{-\infty}^{\infty} \int_{-\infty}^{\infty} Z_{ijl}(k, \omega) U_l(k, \omega) e^{i(kx - \omega t)} dk d\omega. \quad (3)$$



139 **Figure 2.** Wave speeds and impedances for extensional waves (dashed lines) flexural-gravity waves (solid
 140 lines). For the flexural-gravity waves, the curves are calculated for sub shelf cavity thickness $H = 466$ m and
 141 ice thickness $h = 265$ m. All curves are drawn until $hk = 1/2$, reflecting the long wavelength approximation.

154 The exact form of the wave impedance tensor components depends on the type of wave
 155 being considered. For both flexural and extensional waves, the wave impedance is a func-
 156 tion of the wave phase velocity. These wave phase velocities are derived in Appendix B,
 157 and the associated particle motions are described in Appendix C.

158 2.2 Flexural waves

159 The impedance of a wave generally depends on the wave phase velocity $c \equiv \omega/k$.
 160 Writing in terms of the wavelength $\lambda \equiv 2\pi/k$, the phase velocity of flexural-gravity waves
 161 is determined by the dispersion relation

$$\omega^2 = \frac{2\pi g}{\lambda} \frac{(\lambda_{fg}/\lambda)^4 + 1}{2\pi(\rho/\rho_w)h/\lambda + \coth(2\pi H/\lambda)}, \quad (4)$$

162 with water layer thickness H , ice thickness h , acceleration due to gravity g , flexural-gravity
 163 wave length λ_{fg} ,

$$\lambda_{fg} \equiv 2\pi \left(\frac{D}{g\rho_w} \right)^{1/4}, \quad (5)$$

164 flexural rigidity $D \equiv E'h^3$, $E' \equiv E/(1 - \nu^2)$, Young's Modulus E , and Poisson ratio ν . The
 165 material properties of ice are listed in Table 1. At the tip of the Nascent and Loose Tooth
 166 Rifts, $\lambda_{fg} = 7.1$ km and 7.8 km, respectively [Fretwell *et al.*, 2013].

167 The flexural-gravity wave length λ_{fg} separates two regimes of wave behavior (Fig-
 168 ure 2). When $\lambda \gg \lambda_{fg}$ the dispersion relation is identical to that for surface gravity
 169 waves. In contrast, when $\lambda \ll \lambda_{fg}$, the dominant restoring force is elasticity and gravity
 170 does not enter the dispersion relation. As described in detail in Appendix B, this disper-
 171 sion relation is valid for waves with wavelength greater than the ice thickness.

I calculate the flexural mode σ_{xx} -to- u_z impedance component as

$$Z_{xxz}^F = \frac{\Sigma_{xx}}{(-i\omega)U_z} \approx (-i\omega) \frac{hE'}{[c(\omega)]^2}. \quad (6)$$

172 In writing Equation 6, I have used the expressions for the extensional wave stress Σ_{xx} and
 173 vertical displacement U_z derived in Appendix C. The approximate equality symbol reflects
 174 the long wavelength approximation as discussed in Appendix B.

175 This impedance component is plotted in Figure 2. Flexural wave impedance reaches
 176 a maximum at the frequency associated with the flexural-gravity wavelength λ_{fg} . Below
 177 this frequency, impedance increases proportional to frequency ω . Above this frequency,
 178 impedance is a decreasing function of frequency.

179 Flexural stresses, denoted σ_f , may be calculated from a vertical component velocity
 180 seismogram $v_z(t) = \partial u_z / \partial t$ by convolving a velocity time series with the transfer function
 181 in Equation 6,

$$\sigma_f(t) \equiv \sigma_{xx}(t) = E'h \int \frac{(-i\omega)V_z(\omega)}{[c(\omega)]^2} e^{i\omega t} d\omega. \quad (7)$$

182 In this expression I have used the definition of the phase velocity to eliminate reference to
 183 the wavenumber k .

184 A simplified case occurs for wavelengths longer than the water depth H and the
 185 flexural-buoyancy wavelength λ_{fg} . In this case $c^2 = gH$ is nondispersive and therefore
 186 independent of frequency. The integral in Equation 7 may therefore be evaluated as

$$\sigma_f(t) = \frac{E'h}{gH} \frac{\partial V}{\partial t}. \quad (8)$$

187 This result is interesting because it shows that waves in the gravity limit have stresses that
 188 are proportional to particle acceleration. This is in contrast to body waves which have
 189 stresses that are proportional to particle velocity.

2.3 Extensional waves

Extensional waves have nondispersive phase velocity

$$\frac{\omega}{k} = \sqrt{\frac{E'}{\rho}}. \quad (9)$$

This phase velocity is the plane strain equivalent of the wave speed in a one-dimensional elastic bar, $\sqrt{E'/\rho}$. For the material properties of ice (Table 1), this phase velocity is equal to 3375 m/s. The extensional mode does not exhibit any ice–ocean interaction (Appendix A). As was also the case for flexural-gravity waves, this dispersion relation is only valid for waves with wavelength greater than the ice thickness (Appendix B).

The extensional mode has σ_{xx} -to- u_x impedance component,

$$Z_{xxx}^E = \frac{\Sigma_{xx}}{(-i\omega)U_x} \approx -\sqrt{\frac{2\rho\mu}{1+\nu}}. \quad (10)$$

For the material properties of ice $Z_{xxx}^E \approx 2.07$ kPa/(mm/s). This value differs from the corresponding S-wave impedance by a factor of $\sqrt{2/(1+\nu)} \approx 1.23$.

Extensional stresses, denoted σ_e , may be calculated from a horizontal component velocity seismogram $v_x(t) = \partial u_z / \partial t$ as a simple time domain multiplication,

$$\sigma_e(t) \equiv \sigma_{xx}(t) = Z_{xxx}^E v_x(t). \quad (11)$$

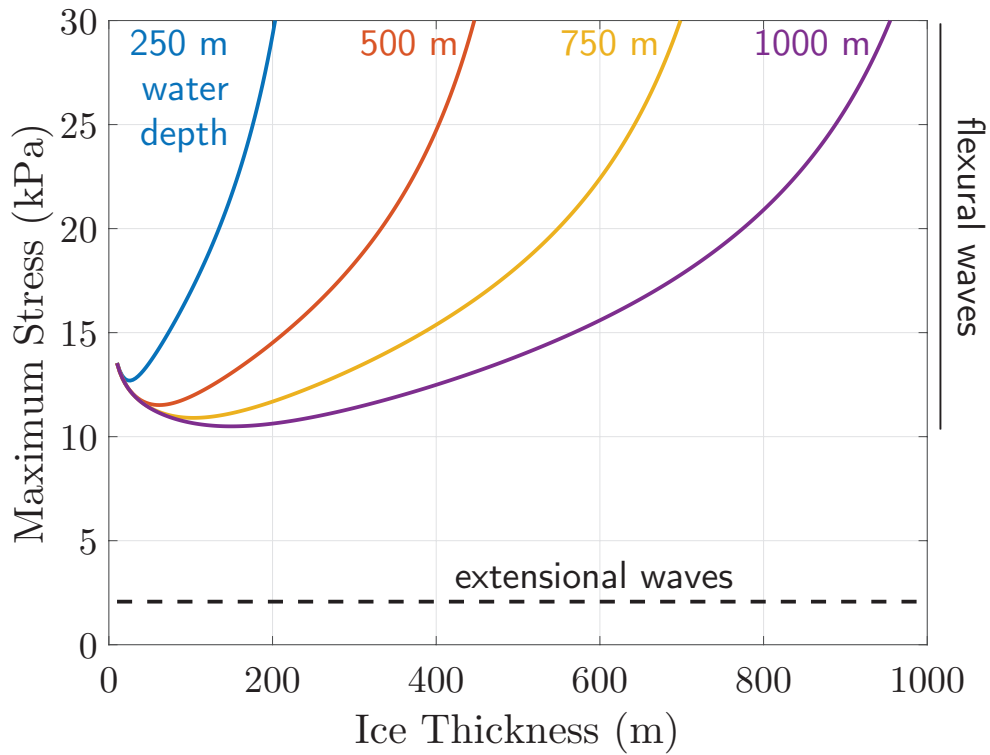
3 Fracture Mechanics

I analyze brittle fracture using the energy-based Griffith fracture criterion [Griffith, 1921] expressed in terms of the stress concentration at the rift tip [Irwin, 1957]. In this description, a preexisting fracture will grow in length when its associated stress intensity factor K exceeds a critical value K_c called fracture toughness, a material property. For ice, K_c ranges between 150 kPa $\sqrt{\text{m}}$ and 400 kPa $\sqrt{\text{m}}$ [Rist *et al.*, 2002]. In Section 6.4 I discuss the uncertainties associated with fracture toughness values.

The model developed in this section depicts the scenario where an ice shelf rift is loaded by wave-induced ocean stresses that are fast enough to be elastic but slow enough that inertia is negligible. As stresses increase over a wave period of tens to hundreds of seconds, the stress concentration at the rift tip increases. Once $K > K_c$, rift tip propagation occurs. In contrast to the loading stage, rift tip propagation may occur sufficiently rapidly so that the rate of propagation becomes limited by the inertia of the ice. Before proceeding with this treatment in Section 3.1, I make two technical notes.

First, I note that inertia is negligible for perturbations with phase velocities far below the elastic waves speeds (see Appendix A). Such perturbations are called quasi-static to reflect that they are time dependent but have negligible inertial influence. In Appendix B, I demonstrate that the quasi-static approximation is valid for ice shelf flexural waves but not for extensional waves because long period extensional waves are not quasi-static. Treating the initiation of propagation as quasi-static is nonetheless a reasonable approximation for the data considered in this paper, however, because in Section 5, I show that flexural stresses are much larger than extensional stresses and therefore are more likely to be responsible for the onset of rift propagation.

Second, I note that the applicability of linear elastic fracture mechanics rests on the condition of small scale yielding. Before continuing I verify this condition. Small scale yield occurs when all dimensions of a fractured object are much greater than the dimension of the plastic region surrounding the rift tip. An estimate of the plastic region size



201 **Figure 3.** Maximum ice shelf stresses generated in response to waves with 0.5 mm/s particle velocity
 202 amplitude. To simulate the effect of ice shelf thinning, curves are calculated for constant ocean floor depth
 203 $H + (\rho/\rho_w)h$ but variable ice thickness h . Stresses refer to the bending stress for flexural waves and the exten-
 204 sional stress for extensional waves. The maximum stress is calculated for each geometry over all wavelengths
 205 λ . The highest flexural wave stress occurs for waves with wavelength λ near the flexural gravity wavelength
 206 λ_{fg} (see Figure 2a).

234 for an ideally elastic-plastic material is [Broek, 2012] $(K_c/\sigma_y)^2$, where $K_c \approx 100$ kPa
 235 $\text{m}^{1/2}$ is the fracture toughness of ice [Rist *et al.*, 2002] and $\sigma_y \approx 100$ kPa is the yield
 236 stress of ice [Van der Veen, 1998]. These estimates give a critical flaw size of about 1 m.
 237 Using a larger fracture toughness of $K_c \approx 400$ kPa $\text{m}^{1/2}$ gives plastic zone size 16 m. For
 238 typical ice shelf thicknesses of one to several hundred meters we may safely proceed with
 239 a plane strain fracture mechanics treatment.

240 3.1 The onset of propagation

241 For a fixed geometry, the stress intensity factor is a linear functional of the stress
 242 tensor. The combined effects of background glacial loading and waves may therefore be
 243 treated by superposition,

$$K = K_{\text{glacial stresses}} + K_{\text{waves}}. \quad (12)$$

244 I treat the situation where the rift stress intensity factor K due to glacier stresses is
 245 lower than the fracture toughness $K < K_c$. This is a reasonable assumption for rifts which
 246 are dormant because under linear elastic fracture mechanics, a crack is expected to have
 247 zero propagation if and only if the stress intensity factor is below the fracture toughness
 248 $K < K_c$. The catalog of rifts published by Walker *et al.* [2013] shows that the majority
 249 of Antarctic rifts are dormant, thus suggesting that the analysis developed here applies
 250 to the majority of Antarctic rifts. For simplicity, I assume that $K_{\text{glacial stresses}} \approx 0$. Rift
 251 propagation would occur at a lower stress than predicted if $K_{\text{glacial stresses}} > 0$.

252 The stress intensity factor due to wave motion may then be broken into flexural and
 253 extensional components,

$$K \approx K_{\text{extension}} + K_{\text{flexure}}. \quad (13)$$

254 The stress intensity factor due to extensional motion is [Broek, 2012],

$$K_{\text{extension}} = \sigma_e \sqrt{\pi L/2}. \quad (14)$$

255 The stress intensity factor due to bending of a buoyantly floating plate is [Bažant,
 256 1992],

$$K_{\text{flexure}} = |\sigma_f| \sqrt{\pi \lambda_{fg}}, \quad (15)$$

257 where the flexural-gravity wavelength is defined in Equation 5. This stress intensity factor
 258 for bending of a floating plate is valid for rifts that are longer than the flexural-gravity
 259 wavelength.

260 3.2 Inertial effects during rift tip propagation

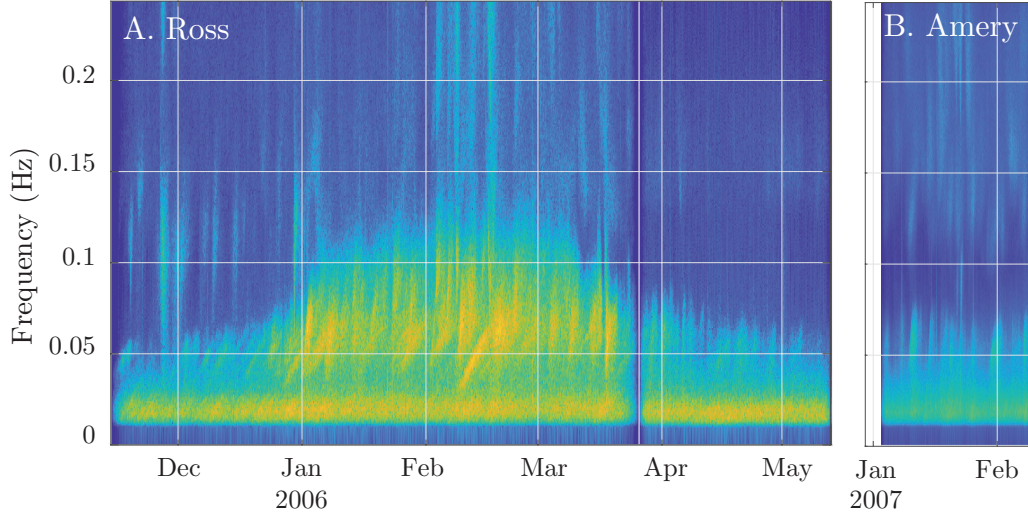
261 The rapid propagation of fractures requires accounting for elastodynamic effects. *Fre-*
 262 *und* [1972a,b] was the first to generalize the analysis of Irwin [1957] to the elastodynamic
 263 case. He found that the stress intensity factor may be written as the product of static and
 264 dynamic terms,

$$K(L, \dot{L}) = \kappa(\dot{L}) K_0(L), \quad (16)$$

265 where an overdot denotes a time derivative. Here, $K_0(L)$ is the time-independent stress
 266 intensity factor, which is identical to the stress intensity factor that would occur due to
 267 loading of a rift with instantaneous length L . The function κ has its origin in a particular
 268 elastodynamic transfer function, and is well approximated by

$$k(\dot{L}) \approx 1 - \frac{1}{c_r} \frac{\partial L}{\partial t}, \quad (17)$$

269 where c_r is the Rayleigh wave speed in ice. The conditions under which Equation 16 is
 270 valid are quite general [Freund, 1998; Rice, 2001]. Specifically, the existence of the fac-
 271 torization of the stress intensity factor into static and dynamic parts is independent of geo-
 272 metric and loading configuration.



283 **Figure 4.** Spectrogram of the data from the Ross (A.) and Amery (B.) Ice Shelves. Upward sloping spectral
 284 bands show the arrival of ocean swell from distant storms [Cathles *et al.*, 2009]. Both datasets are plotted
 285 with the same log-power color scale.

273 Combining Equations 16 and 17 gives the rift tip equation of motion

$$\frac{\partial L}{\partial t} = \begin{cases} c_r \left[1 - \left(\frac{K_c}{K} \right)^2 \right] & K \geq K_c \\ 0 & K < K_c \end{cases} \quad (18)$$

274 This result has general features which have been noted previously [Freund, 1998], but are
 275 worth highlighting. In particular, the crack tip velocity has an instantaneous dependence
 276 on the stress level through the stress intensity factor K . This instantaneous response re-
 277 sults because there is no sensitivity to the second derivative of L in Equation 18. Integrat-
 278 ing the rift tip velocity gives the rift propagation distance,

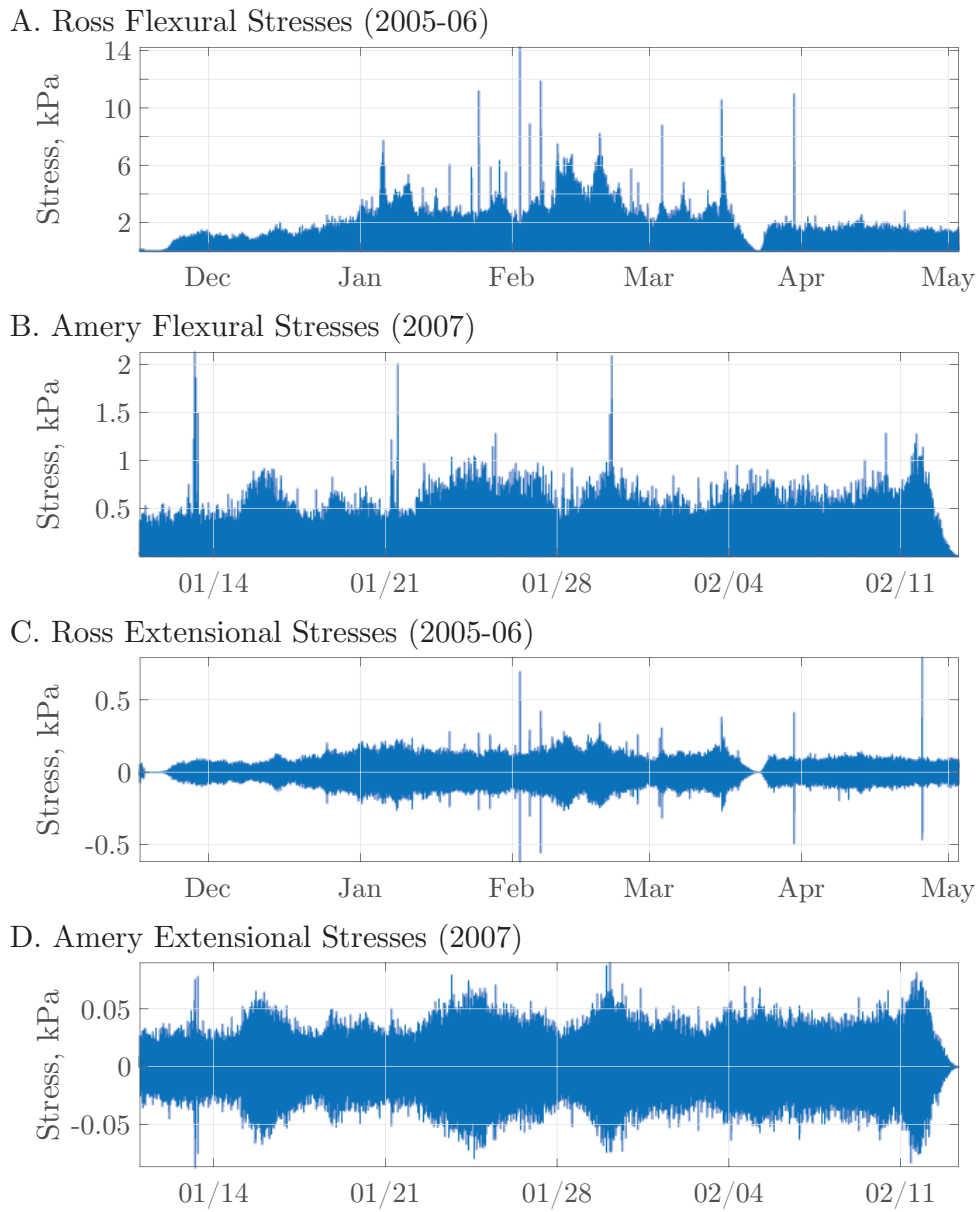
$$\delta L(t) = c_r \int_0^t \left\{ 1 - \frac{K_c [L(t')]}{K[\sigma(t'), L(t')]} \right\} dt'. \quad (19)$$

279 I note that this description accounts for spatial variability in fracture toughness due, for
 280 example, to the presence of high toughness suture zones with accreted basal marine ice
 281 [Holland *et al.*, 2009; McGrath *et al.*, 2012; Jansen *et al.*, 2013; LeDoux *et al.*, 2017].

282 4 Observations of the Loose Tooth and Nascent Rifts

288 4.1 Rift propagation behavior

289 In this paper I analyze two rifts, the Nascent Iceberg Rift on the Ross Ice Shelf and
 290 the Loose Tooth T2 Rift on the Amery Ice Shelf. I focus on observation periods during
 291 which seismic data is available: November 2005 to May 2006 on the Ross Ice Shelf and
 292 January to February 2007 on the Amery Ice Shelf. During these times, the Loose Tooth
 293 and Nascent Rifts were 17 and 46 km long [Scambos *et al.*, 2007]. The tip of the Nascent
 294 Rift was located in ice with thickness $h = 265$ m. The ocean floor was 691 m below sea
 295 level and the sub shelf cavity was therefore $H = 479$ m thick. The tip of the Loose Tooth
 296 Rift was located in ice with thickness $h = 301$ m. The ocean floor was 734 m below sea
 297 level and the sub shelf cavity was therefore $H = 466$ m thick. These geometries are com-
 298 pared in Figure 1.



286

Figure 5. Calculated wave stresses on the Ross and Amery Ice Shelves. Note the different horizontal and vertical axes.

287

299 During these time periods, neither rift exhibited measurable rift propagation. This is
 300 probably due to the fact that both rifts have propagated into ice suture zones that appar-
 301 ently have higher fracture toughness than the surrounding ice shelf [Borstad *et al.*, 2017].
 302 I reach these conclusions by examining satellite imagery as archived in the Antarctic Ice
 303 Shelf Image Archive at the National Snow and Ice Data Center [Scambos *et al.*, 2009b].
 304 These images are captured using the Moderate Resolution Imaging Spectroradiometer
 305 (MODIS) instrument. The observation that the Amery did not exhibit propagation dur-
 306 ing this time has been previously noted by Walker *et al.* [2015]. The nominal resolution
 307 of 250 m places an upper bound on the amount of propagation that could go undetected,
 308 although because of uncertainties in image analysis Walker *et al.* [2015] uses a great un-
 309 certainty of 1 km, which I adopt here.

310 4.2 Seismic data

311 I analyze continuously recorded seismograms from seismometers on the Ross and
 312 Amery Ice Shelves, Antarctica. These data sets were previously described by MacAyeal
 313 *et al.* [2006] and Cathles *et al.* [2009] and by Bassis *et al.* [2008], respectively. I obtain
 314 all seismograms from the Incorporated Research Institutions for Seismology (IRIS) Data
 315 Management Center website. The locations of the seismometers used in this study are
 316 shown in Figure 1.

317 On the Ross Ice Shelf I examine data from the station RIS2, temporary network
 318 code XV, during the 2005-2006 deployment [MacAyeal *et al.*, 2006]. RIS2 was located
 319 several km from the tip of the Nascent Rift. From this deployment there are 167 d of
 320 data with one outage of several days in late March 2006. On the Amery Ice Shelf I ex-
 321 amine data from the station BFN1, temporary network code X9, during a deployment in
 322 January 2007. From this deployment there are 36 d of data. Although many other instru-
 323 ments were deployed over a period of several years, I focus on this station because it uses
 324 a Guralp CMG-40T seismometer while most other stations use Mark Products L28 seis-
 325 mometers. The CMG-40T has a flat instrumental response down to 0.03 Hz and is there-
 326 fore expected to be better suited for measuring ocean waves with typical periods of several
 327 seconds.

328 Inferring stresses from seismograms requires interpreting the amplitude information
 329 contained in seismic traces. The issue of instrumental response therefore requires special
 330 attention. Seismometers have reduced sensitivity to motions below the instrumental sen-
 331 sitivity frequency. When the instrument response is deconvolved from a discretized volt-
 332 age trace (with units of counts), this insensitivity results in division by a small number,
 333 thereby amplifying small amounts of noise. Although geophysically interesting informa-
 334 tion may be contained at frequencies lower than the instrumental sensitivity frequency, in
 335 this study I take a conservative approach and only interpret features in seismograms that
 336 occur at frequencies above the sensitivity frequency. I first taper and then bandpass fil-
 337 ter all raw seismic traces. The bandpass filter has cutoff frequencies 0.01, 0.02, 0.2, and
 338 0.4 Hz. I then remove the instrumental response from all seismograms. In all of my anal-
 339 ysis I focus on the LH channels that are sampled at 1 Hz.

340 Spectrograms of the waveforms used in this study shown in the spectrogram in Fig-
 341 ure 4. The principal feature is the arrival of ocean swell from distant storms. These storm
 342 waves appear as upward sloping spectral lines. This occurs because long period ocean
 343 swell travels faster and therefore arrives before short period swell [Munk *et al.*, 1963].
 344 This signal has been described extensively by Cathles *et al.* [2009] and the interested reader
 345 is referred there for more details.

5 Analysis of seismic data from the Ross and Amery Ice Shelves

5.1 Wave-induced stresses

Using the data described in Section 4.2, I estimate flexural stresses σ_f using Equation 7 and extensional stresses σ_e using Equation 11. There are two primary results (Figure 5). First, wave stresses are much greater on the Ross Ice Shelf than on the Amery Ice Shelf. Second, on both the Amery and the Ross Ice Shelf, flexural waves carry greater stresses than extensional waves. These two patterns are true of the peak stresses as well as the root mean squared (RMS) averaged stresses. The largest observed flexural and extensional stresses on the Ross Ice Shelf were 14.2 and 0.8 kPa, respectively. On the Amery Ice Shelf, the largest observed flexural and extensional stresses were 2.1 and 0.09 kPa, respectively. The RMS flexural and extensional stresses on the Ross Ice Shelf were 0.6 kPa and 0.03 kPa. The RMS flexural and extensional stresses on the Amery were 0.2 kPa and 0.01 kPa.

The most likely reason for the higher observed wave stresses on the Ross Ice Shelf compared to the Amery is that the Ross seismograms are much longer (167 d) than the Amery seismograms (36 d) and were therefore able to record a wider range of variability in ocean wave activity. To test this hypothesis, I examine the most quiet period during the Ross deployment, December 2005. I refer to this as the Ross quiet period. I find that the wavefield stresses during the Ross quiet period were similar to those on the Amery Ice Shelf. During the Ross quiet period, the maximum inferred flexural and extensional stresses were 2.0 kPa and 0.13 kPa, respectively.

Flexural waves carried greater stresses than extensional waves during the two observation periods. The Ross Ice Shelf wave field had extensional waves with greater particle velocity amplitude than flexural wave particle velocity amplitude by a factor of three [Bromirski *et al.*, 2010, 2015, 2017]. These two waves, however, have different wave impedances. As a result, the larger stress need not be caused by the larger particle velocity.

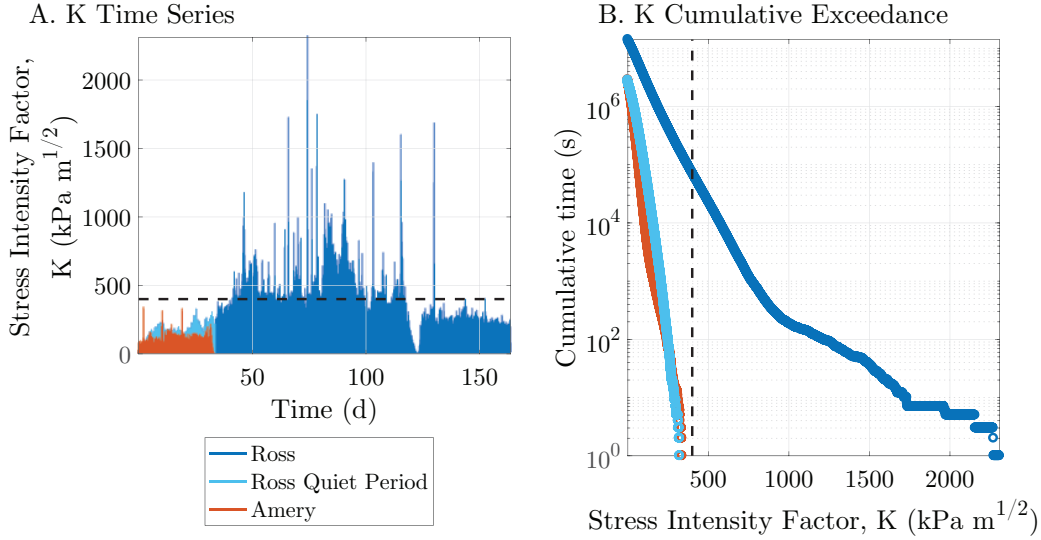
5.2 Rift propagation

Using the estimated stresses, I calculate the stress intensity factor K using Equation 13. There are two main results. The first result is that waves stresses were exceeded the fracture criterion on the Ross Ice Shelf but not on the Amery Ice Shelf (Figure ??). As discussed later (Section 6.4), I assume a fracture toughness $K_c = 400 \text{ kPa}\sqrt{\text{m}}$ to represent tough suture zones with accreted basal marine ice. With this fracture toughness, I predict that rift propagation was possible for a cumulative total of $\sim 10^4$ s during the Ross Ice Shelf observation period. On the Amery Ice Shelf and during the quiet period on the Ross Ice Shelf, I predict that wave stresses were not large enough to induce propagation.

The second result is that, in the absence of any other resistance to rift propagation, the inferred wave-induced stresses are predicted to have caused much more propagation than was actually observed. I use the integral in Equation 19 to calculate rift tip propagation distances. On the Ross Ice Shelf, a fracture toughness $K_c = 400 \text{ kPa}\sqrt{\text{m}}$ results in a physically unrealistic 10^6 km of rift tip propagation. Actual rift propagation was measured to have been less than 1 km during the observation period (Section 4). Motivated by this discrepancy, I next consider several possible sources of resistance to ice shelf rift propagation.

5.3 Rift cohesive strength

In order to match the observed lack of rift propagation, I consider two additional types of rift strength. First, I consider the situation discussed by Bassis *et al.* [2007] where the fracture toughness experiences an increase by an amount Δ to a new value $K_c + \Delta$. This perturbed value could equally well represent fracture toughness variation in space or



414 **Figure 6.** Comparison of the wave-induced stress intensity factor on the Ross (blue) and Amery (red) Ice
 415 Shelves. During the time of minimal wave activity on the Ross Ice Shelf (light blue), wave stresses were
 416 comparable to those observed on the Amery Ice Shelf. The stress intensity factor was computed from seis-
 417 mograms using Equation 13 and does not account for cohesive strengthening (Section 5.3). The dashed
 418 lines shows the fracture toughness K_c and therefore the value of the stress intensity factor K at which rift
 419 propagation is predicted to occur.

394 in time. Returning to the calculation in the previous section, I find that a value of $\Delta =$
 395 $1600 \text{ kPa}\sqrt{\text{m}}$ is necessary to match the observation that less than 1 km of propagation
 396 occurred. This value results in a total ice fracture toughness $\sim 2 \text{ MPa}\sqrt{\text{m}}$, which is an
 397 order of magnitude higher than typical laboratory-derived values [Rist *et al.*, 2002]. For
 398 this reason, I consider variable fracture toughness to not be a viable mechanism to explain
 399 the observed rift behavior.

400 As a second strengthening mechanism, I consider the cohesive effect of refrozen
 401 melange and sea ice between the rift walls. The stress intensity factor due to a uniformly
 402 applied stress acting to resist rift opening is the same as in Equation 14 but with opposite
 403 sign [Sih, 2012],

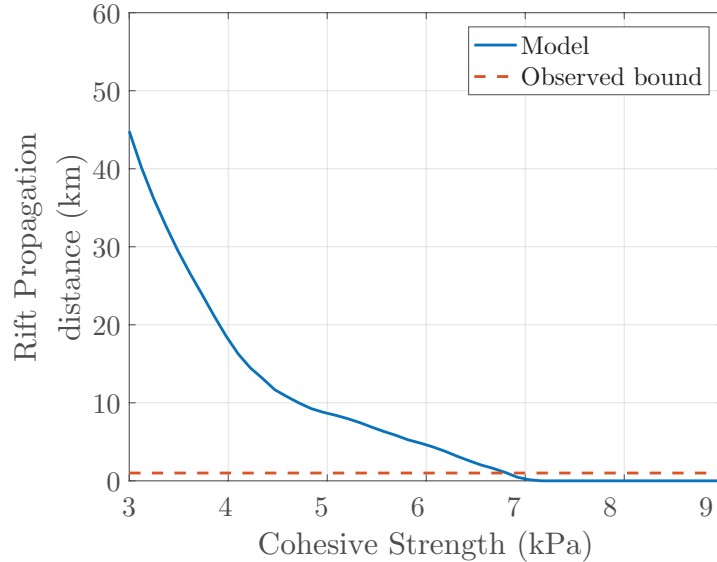
$$K_{\text{cohesion}} = -\sigma_c \sqrt{\pi L/2}, \quad (20)$$

404 where σ_c is defined here to be the stress due to cohesive melange and sea ice that act to
 405 “glue” the rift walls together. Equation 13 then becomes,

$$K \approx \max [K_{\text{extension}} + K_{\text{flexure}} + K_{\text{cohesion}}, 0]. \quad (21)$$

406 The maximum function is applied because the cohesive strength does not result in a neg-
 407 ative stress intensity factor K . A negative K would imply closing motion of the rift walls.
 408 Instead, a cohesive stress is generated only in response to wave stresses and therefore
 409 never results in negative K .

410 I find that a cohesive stress $\sigma_c = 6.8 \text{ kPa}$ is the minimum required cohesive stress
 411 necessary to produce $\delta L < 1 \text{ km}$. This result is plotted in Figure ??, which plots the pre-
 412 dicted amount of rift propagation as a function of the cohesive strength of the rift. In the
 413 Section 6.5 I discuss several interpretations of this cohesive stress.



420 **Figure 7.** The predicted rift propagation decreases as the rift cohesive strength increases. Satellite imagery
 421 shows less than 1 km of propagation, therefore suggesting a cohesive strength of 6.8 kPa. The blue curve was
 422 calculated using Equations 19 and 21.

423 6 Discussion and Conclusions

424 6.1 Uncertainties in the calculation of wave-induced stresses

425 I have calculated ice shelf stresses from seismic data and related these stresses to
 426 a fracture criterion. Although I have made several simplifying assumptions, the stresses
 427 that I estimate are nevertheless in reasonable agreement with previous studies. *Sergienko*
 428 [2017] for example, used the BEDMAP2 geometry from the Ross Ice Shelf but employing
 429 an idealized wave forcing, calculated flexural stresses in the range of 0-15 kPa. In compar-
 430 ison, I find a RMS and peak wave stress on the Ross Ice Shelf of 0.8 and 17.5 kPa. The
 431 principal differences from the results of *Sergienko* [2017] are related topographic focus-
 432 ing. I treat a simplified two-dimensional geometry where the ice shelf is infinitely long
 433 and wide, small ice shelves of comparable dimension to the flexural gravity length scale
 434 are expected to significantly deviate from the predictions made in this paper. One reason
 435 for this is that tidal stresses, for example, become significant within a distance from the
 436 grounding line that scales with λ_{fg} [*Holdsworth, 1969; Vaughan, 1995*].

437 6.2 Can ocean waves trigger rift propagation?

438 To the best of my knowledge, no previous study has definitively demonstrated that
 439 ocean waves may trigger ice shelf rift propagation. To address this situation, I have at-
 440 tempted in this paper to construct a simple model of wave-induced rifting. Although I
 441 have been able to make this model behave in a manner consistent with observed rift be-
 442 havior, no large rift propagation event occurred during the period from which I have data.
 443 As a result, definitive proof of ocean wave triggering remains elusive. This result empha-
 444 sizes the importance of ongoing seismological fieldwork on ice shelves [*Banwell et al.,*
 445 *2017; Bromirski et al., 2017*]. Additional fieldwork would clarify other issues as well. Al-
 446 though I show that a period of low wave activity on the Ross is comparable to the Amery
 447 record, further observations are needed to confirm whether activity on the Amery –or any

448 other ice shelf for that matter— ever reaches stress levels as high as those observed on the
449 Ross.

450 **6.3 Other mechanisms of episodic rift extension**

451 *Larour et al.* [2004a], citing laboratory studies such as those by *DeFranco and Dempsey*
452 [1994], invokes constitutive instability as a possible mechanism for episodic rift activity.
453 Constitutive instability gives rise, for example, to the stick-slip instability that is respon-
454 sible for basal stick slip motion of glaciers and ice sheets [*Lipovsky and Dunham*, 2016,
455 2017]. Such behavior is a typical pathology of laboratory experiments conducted on sam-
456 ples which are too thin to achieve a state of plane strain [*Bažant*, 1993; *Broek*, 2012]. As
457 discussed in Section 3, ice shelf rifts are expected to occur in ice that is thick enough to
458 be in plane strain. This type of behavior is therefore expected to occur in thinner bodies
459 of floating ice such as sea ice [*DeFranco and Dempsey*, 1994]. Furthermore, a constitutive
460 instability hypothesis is appealing in situations such as the tectonic earthquake cycle where
461 the loading applied to a system is known to be approximately constant in time. The find-
462 ing from the present study, that wave-induced loading is highly time dependent, suggests
463 that constitutive instability, though possible, is not a strictly necessary condition to explain
464 episodes of ice shelf rift propagation.

465 **6.4 The fracture toughness of ice shelf suture zones**

466 I have chosen a value $K_c = 400 \text{ kPa}\sqrt{\text{m}}$ to represent the fracture toughness of ice
467 shelf suture zones. This choice is based on the best available laboratory data [*Rist et al.*,
468 2002], and was chosen to be at the high end of laboratory data to reflect the fact that su-
469 ture zones appear to be more resistant to rift propagation than the surrounding ice shelf
470 [*Holland et al.*, 2009; *McGrath et al.*, 2012; *Jansen et al.*, 2013; *LeDoux et al.*, 2017]. I
471 also invoke the laboratory measurements to support the claim that fracture toughness vari-
472 ations cannot entirely be responsible for the observed response of the Nascent Iceberg Rift
473 to wave-induced stresses. An important caveat to these statements is that, to my knowl-
474 edge, no ice core has ever been collected from an ice shelf suture zones. Fracture tough-
475 ness measurements from *in situ* suture zone ice cores could therefore support or refute
476 these ideas. The exact micromechanical processes that result in the apparently elevated
477 fracture tough of ice shelf suture zones remain unknown [*McGrath et al.*, 2014].

478 **6.5 Cohesive rift strengthening**

479 My description of rift propagation mechanics predicts that wave stresses would have
480 caused calving of a tabular iceberg in the absence of additional sources of rift strength.
481 Previous studies have suggested a role for melange dynamics as a rift strengthening mech-
482 anism [*MacAyeal et al.*, 1998; *Rignot and MacAyeal*, 1998; *Larour et al.*, 2004b; *Fricker*
483 *et al.*, 2005]. For simplicity I have quantified this stabilizing tendency as a force applied
484 uniformly over the entire rift length. This rift strengthening can equivalently be thought
485 of as a cohesive zone [*Rice*, 1968]. I have not attempted to quantify the spatial variation
486 of rift strengthening; it may be the case that rift strengthening is localized to the near-tip
487 region [*Dugdale*, 1960; *Barenblatt*, 1962]. Near-tip localization of cohesive strength to a
488 process-zone region [*Broek*, 2012] could result from the effect of bottom crevasses form-
489 ing ahead of the rift tip [*Rice and Levy*, 1972] or because of rift tip blunting [*Larour et al.*,
490 2004b].

491 **6.6 Response to melange and ice shelf thinning**

492 The rift model presented here suggests at several possible effects related to ice shelf
493 and melange thinning. First, the result of Section 5.3 suggests that rift-filling melange
494 may stabilize rift propagation. Reduced melange may therefore weaken ice shelves by

495 destabilizing rift propagation [Rignot and MacAyeal, 1998; MacAyeal *et al.*, 1998]. The
 496 wave response to thinning, in contrast, is stabilizing. Stabilization occurs for two reasons.
 497 First, the flexural-gravity wavelength (Equation 5) is expected to decrease. This results
 498 in a lower stress concentration due to flexural waves (Equation 15). Second, the flexural
 499 wave impedance is a increasing function of ice thickness (Figure 3). Thus thinning of an
 500 ice shelf is expected to lower wave stresses. Both of these stabilizing effects occur because
 501 thin ice shelves are more compliant and more compliant structures are less susceptible to
 502 brittle fracture. Further observations, both seismic and remotely sensed, are need to quan-
 503 tify whether the destabilization due to melting and warming is greater than the stabiliza-
 504 tion due to thinning.

505 **6.7 The Loose Tooth Rift: stabilization due to propagation into deeper water?**

506 The location where the Loose Tooth T2 Rift intersects the ice front, i.e. where the
 507 rift initiated, occurs in a part of the shelf that is above shallow water ($H = 253$ m).
 508 The rift has subsequently propagated into a part of the shelf that is above deeper water
 509 ($H = 466$ m). The ice thickness at the front is similar to the ice thickness at the current
 510 rift tip ($h = 265$ m versus $h = 301$ m). Carrying out a calculation of maximal flexu-
 511 ral stress similar to Figure 3, I find that waves with identical particle velocity amplitudes
 512 would induce stresses approximately 27% higher at the ice front versus the current rift
 513 tip. Observed wave-induced stresses on the Amery were very near the failure criterion
 514 (Figure ??b). This result suggests that the Loose Tooth T2 Rift was more susceptible to
 515 wave-induced stresses during its initial formation in shallow water, and that propagation
 516 into deeper water may have stabilized the rift tip in its current position. As noted above,
 517 this hypothesis is not strictly testable because there were no seismometers deployed on the
 518 Amery during the initial formation of the Loose Tooth T2 Rift. Future seismic deploy-
 519 ments would therefore be useful because they could clarify whether stabilization due to
 520 propagation into deeper water is an important process.

521 **7 Conclusions**

522 I propose a simple rift propagation criterion based on the observation that most ice
 523 shelf rifts show extended periods of dormancy and therefore must have low background
 524 stress concentrations. This low background stress concentration makes ice shelf rifts sus-
 525 ceptible to wave-induced stresses. I infer that a cohesive strengthening of the rift, possibly
 526 due to refrozen melange, counteracts this destabilizing tendency. I relate this description
 527 of rift propagation to *in situ* ice shelf stresses inferred using passive seismology. By infer-
 528 ring stresses associated with rift propagation, this work addresses a basic limitation in our
 529 understanding glacier calving physics: specifically, knowledge of the state of stress at the
 530 site of fracture [Benn *et al.*, 2007]. This study therefore offers a detailed glimpse into the
 531 mechanics of a particular type of glacier calving, ice shelf rift propagation.

532

A: Governing Equations

533

534

535

536

537

538

The propagation of ocean waves in floating ice shelves has received extensive treatment. The flexural motions of an elastic bar were first examined by *Greenhill* [1886]. This analysis was generalized to extensional motions by [*Press and Ewing*, 1951, but see also literature cited therein]. The main reason that I repeat the analysis of [*Press and Ewing*, 1951] is to obtain self-consistent expressions for the particle velocities, stresses, and dispersion relations that were not explicitly given by [*Press and Ewing*, 1951].

539

A.1 The elastic ice layer

I consider a coordinate system with the z direction being positive upwards and x being positive in the direction of ice flow. An ice layer that is initially at rest and everywhere at overburden pressure occupies the region between $z = 0$ and $z = -h$. The entire geometry is assumed to be translationally invariant in the x direction, and I take $u_y = \partial/\partial y = 0$ so that deformations are in a state of plane strain. Perturbations to this initial state obey the momentum balance equations,

$$\rho \frac{\partial^2 u_x}{\partial t^2} = \frac{\partial \sigma_{xx}}{\partial x} + \frac{\partial \sigma_{xz}}{\partial z}, \quad (\text{A.1})$$

$$\rho \frac{\partial^2 u_z}{\partial t^2} = \frac{\partial \sigma_{xz}}{\partial x} + \frac{\partial \sigma_{zz}}{\partial z}, \quad (\text{A.2})$$

540

541

for ice density ρ and stress tensor σ_{ij} . Stresses are related to displacement gradients through the constitutive relationship [*Malvern*, 1969],

$$\sigma_{ij} = \lambda \left(\frac{\partial u_k}{\partial x_k} \right) \delta_{ij} + \mu \left(\frac{\partial u_i}{\partial x_j} + \frac{\partial u_j}{\partial x_i} \right), \quad (\text{A.3})$$

542

543

where, for simplicity, elastic anisotropy is neglected. The values of elastic moduli, here written using Lamé's parameter λ and the shear modulus μ , are given in Table 1.

Applying the transform of Equation 2 to the governing equations (Equations A.1-A.3) gives rise to a system of two coupled ordinary differential equations with derivatives in z . These equations have solution [*Graff*, 2012],

$$U_x = ik (A \sin \alpha z + B \cos \alpha z) + i\beta (C \cos \beta z - D \sin \beta z), \quad (\text{A.4})$$

$$U_z = \alpha (A \cos \alpha z - B \sin \alpha z) + k (C \sin \beta z + D \cos \beta z), \quad (\text{A.5})$$

where,

$$\alpha = k \sqrt{\left(\frac{\omega}{kc_p} \right)^2 - 1}, \quad (\text{A.6})$$

$$\beta = k \sqrt{\left(\frac{\omega}{kc_s} \right)^2 - 1}. \quad (\text{A.7})$$

544

545

Here, c_p and c_s are the p- and s-wave speeds in the ice (see Table 1). The quasi-static limit occurs when $\omega/(kc_p) \ll 1$ and $\omega/(kc_s) \ll 1$. In this case $\alpha \approx \beta \approx k$.

The boundary conditions at the ice-atmosphere boundary $z = 0$, are

$$\sigma_{xz}(z = 0) = 0, \quad (\text{A.8})$$

$$\sigma_{zz}(z = 0) = 0. \quad (\text{A.9})$$

546

Two other boundary conditions are required, and these occur at the ice-ocean interface.

547

A.2 Ice–ocean coupling

548

549

The unperturbed ice–ocean interface is located at $z = -h/2$. The ice–ocean boundary moves in response to perturbations, with the deformed interface located at

$$z = -h + \phi(x, t). \quad (\text{A.10})$$

Consistent with a linearized theory of wave propagation, I assume that such geometric changes are small and following standard treatments [*Lipovsky and Dunham, 2015; Gill, 2016*] I prescribe boundary conditions on the undeformed interface. At this boundary, the force exerted on the ice by the water $\delta p(x, t)$ is equal and opposite to the force exerted by the water on the ice σ_{zz} ,

$$\sigma_{zz}(-h) = -\delta p(x, t). \quad (\text{A.11})$$

The ocean is treated as inviscid so there is no shear stress,

$$\sigma_{xz}(-h) = 0. \quad (\text{A.12})$$

And by continuity the velocities must match between the fluid and solid,

$$\frac{\partial u_z}{\partial t}(-h) = v_z, \quad (\text{A.13})$$

550

551

552

where v_z is the vertical fluid velocity. I next examine motions in the sub-ice ocean waters with the goal of describing the fields δp and v_z (Equations A.11 and A.13) on the ice–ocean interface.

553

A.3 Sub-ice-shelf cavity circulation

554

555

I examine the behavior of perturbations to a sub-ice shelf cavity initially at rest. In this initial state, the pressure in the water is,

$$p_0(z) = \rho_w g(z + h) + \rho_w g h. \quad (\text{A.14})$$

556

I then define the total fluid pressure p' to be

$$p'(x, z, t) = p(x, z, t) + p_0(z) \quad (\text{A.15})$$

Flow perturbations follow the linearized equations for an incompressible, inviscid flow with uniform density. The horizontal and vertical momentum balance equations are

$$\rho_w \frac{\partial v_x}{\partial t} = -\frac{\partial p}{\partial x} \quad (\text{A.16})$$

$$\rho_w \frac{\partial v_z}{\partial t} = -\frac{\partial p}{\partial z}. \quad (\text{A.17})$$

557

Here v_x and v_z are the x - and z -components of fluid velocity.

558

559

I assume that the ocean waters are of uniform density so that the ocean water mass conservation equation is

$$\frac{\partial v_x}{\partial x} + \frac{\partial v_z}{\partial z} = 0. \quad (\text{A.18})$$

560

561

This statement of mass conservation may be combined with Equations A.16 and A.17 with the result being Laplace's equation for pressure,

$$\nabla^2 p = 0. \quad (\text{A.19})$$

562

563

The fluid flow is irrotational as a consequence of the inviscid, uniform density, and small perturbation assumptions [*Gill, 2016, Section 5.2*].

564 The boundary condition at the ocean bottom, $z = -h - H$, is that vertical velocities
565 vanish,

$$v_z(z = -h - H) = 0. \quad (\text{A.20})$$

566 At the ice–ocean interface, the water pressure perturbation is approximately equal to
567 the hydrostatic pressure at the deformed ice–ocean interface location ϕ plus the pressure
568 exerted by the ice on the water,

$$p(-h) = \rho_w g \phi(x, t) + \delta p(x, t). \quad (\text{A.21})$$

The fluid equations (A.19-A.21) may be solved in the transform domain using Equation 2. The result is a transfer function between ΔP and surface height Φ ,

$$\Delta P = \rho_w g \left(\frac{\omega^2}{gk} \coth(kH) - 1 \right) \Phi \equiv -T(k, \omega) \Phi. \quad (\text{A.22})$$

569 I again apply the convention from the main text that capital letters denote Fourier trans-
570 formed quantities.

The transfer function of Equation A.22, combined with the the ice–ocean coupling conditions (Equations A.11 and A.13), allows me to write the entire coupled ice–ocean problem exclusively in terms of boundary conditions on the elastic solid. In Equation A.22, ΔP and Φ can be eliminated in favor of the field variables Σ_{zz} and U_z , defined in the elastic solid. The result is the bottom boundary conditions on the elastic ice layer,

$$\Sigma_{zz}(z = -h) = T(k, \omega) U_z(z = -h), \quad (\text{A.23})$$

$$\Sigma_{xz}(z = -h) = 0. \quad (\text{A.24})$$

571 It is interesting to note that ice–ocean coupling manifests itself as the condition in Equa-
572 tion A.23, namely, as a Robin type boundary condition that relates the vertical elastic dis-
573 placement to the vertical compressive elastic stress.

574 A.4 The dispersion relation

The four boundary conditions (Equations A.8, A.9, A.23, and A.24) on the elastic solid result in a homogeneous system of equations,

$$\left\{ \begin{array}{cccc} 2(k^2 - \beta^2) \mu \cos(h\alpha) & 4k\beta\mu \cos(h\beta) & 0 & 0 \\ 2k\alpha \sin(h\alpha) & (\beta^2 - k^2) \sin(h\beta) & 0 & 0 \\ 0 & 0 & 4k\beta\mu \sin(h\beta) & 2(\beta^2 - k^2) \mu \sin(h\alpha) \\ 0 & 0 & (k^2 - \beta^2) \cos(h\beta) & 2k\alpha \cos(h\alpha) \end{array} \right\} -T \left[\begin{array}{cccc} \alpha \sin(h\alpha) & -k \sin(h\beta) & k \cos(h\beta) & \alpha \cos(h\alpha) \\ 0 & 0 & 0 & 0 \\ \alpha \sin(h\alpha) & -k \sin(h\beta) & k \cos(h\beta) & \alpha \cos(h\alpha) \\ 0 & 0 & 0 & 0 \end{array} \right] \begin{pmatrix} B \\ C \\ D \\ A \end{pmatrix} = \begin{pmatrix} 0 \\ 0 \\ 0 \\ 0 \end{pmatrix} \quad (\text{A.25})$$

575 Solutions to these equations require a vanishing determinant, and this condition
576 gives rise to the dispersion relation,

$$D(k, \omega) = D_E(k, \omega) D_F(k, \omega) + D_{HD}(k, \omega) = 0. \quad (\text{A.26})$$

where,

$$D_F \equiv \frac{\tan(\alpha h)}{\tan(\beta h)} + \frac{(k^2 - \beta^2)^2}{4\alpha\beta k^2}, \quad (\text{A.27})$$

$$D_E \equiv \frac{\tan(\alpha h)}{\tan(\beta h)} + \frac{4\alpha\beta k^2}{(k^2 - \beta^2)^2}, \quad (\text{A.28})$$

$$D_{HD} \equiv \frac{T}{2\mu} \frac{\alpha(\beta^2 + k^2) [\tan^2(\alpha h) - 1]}{4\alpha\beta k^2 \tan(\beta h)} \left[\frac{\tan^2(\beta h) - 1}{\tan^2(\alpha h) - 1} + \frac{\tan(\alpha h)}{\tan(\beta h)} \frac{4\alpha\beta k^2}{(k^2 - \beta^2)^2} \right]. \quad (\text{A.29})$$

577 The subscript *HD* stands for hydrodynamic. Terms with this subscript are related to flow
578 in the sub shelf cavity.

579 When ice–ocean coupling is absent, $T = 0$ and so $D_{HD} = 0$. In this case Equa-
580 tion A.26 reduces to the Lamb wave dispersion relation. This dispersion relation corre-
581 sponds to the motions of an elastic layer with zero stress boundary conditions [*Graff*,
582 2012]. The Lamb wave dispersion relation is notable because it consists of uncoupled
583 flexural and extensional modes. Mathematically this uncoupling occurs because it is possi-
584 ble to factor the dispersion relation into the product of two terms, D_E and D_F . Equa-
585 tion A.26 is equivalent to Equation 49 of *Wang and Shen* [2010] in the case of a perfectly
586 elastic ice layer.

587 In general, the mechanical interaction that occurs at the ice–ocean interface results
588 in coupling between the flexural and extensional motions of the ice shelf. For this reason,
589 there are no longer uncoupled flexural and extensional modes over the entire frequency-
590 and wavenumber-spectra as there is in the more specific Lamb wave case. I will show in
591 the next section, however, that for wavelengths that are long compared to the ice thickness,
592 a simplification to extensional and flexural modes occurs.

593 B: The long wavelength limit

The observed seismic spectrum on the Ross and Amery Ice Shelves is dominated
by wave energy at frequencies lower than several seconds (Figure 4). Using the dispersion
relations for extensional (Equation 9) and flexural wave motions (Equation 4), I calculate
that these waves correspond to waves with wavelength of at least several kilometers. This
observation motivates a more careful examination of waves with wavelength that are much
longer than the ice shelf thickness. I calculate the Taylor series in the small parameter kh
for the dispersion relation of Equation A.26,

$$D_F \approx \frac{1}{12} \left(\frac{\omega}{kc_s} \right)^2 \left\{ \frac{\omega^2}{c_s^2 k^2} \left[\frac{1}{2} (\gamma^2 - 1)^2 h^2 k^2 - 3 \right] + (\gamma^2 - 1) h^2 k^2 \right\}, \quad (\text{B.1})$$

$$D_E \approx \frac{1}{4} \left(\frac{\omega}{kc_s} \right)^2 \left[4(\gamma^2 - 1) + (2\gamma^4 - 1) \frac{\omega^2}{c_s^2 k^2} \right], \quad (\text{B.2})$$

$$D_{HD} \approx \frac{T}{\mu h k^2} \frac{1}{4} \left(\frac{\omega}{kc_s} \right)^4 \left[4(\gamma^2 - 1) + (2\gamma^4 - 1) \frac{\omega^2}{c_s^2 k^2} \right] \left[\frac{\gamma^2 + 1}{2} \frac{\omega^2}{k^2 c_s^2} + 1 \right]. \quad (\text{B.3})$$

I have defined $\gamma \equiv c_s/c_p$. The resulting expression for the dispersion relation permits
factorization into the form,

$$\begin{aligned} D(k, \omega) \approx & \left(\frac{\omega}{c_s k} \right)^4 \left\{ 4(\gamma^2 - 1) + (2\gamma^4 - 1) \left(\frac{\omega}{c_s k} \right)^2 \right\} \\ & \times \left\{ (\gamma^2 - 1) h^2 k^2 + \frac{3T}{\mu h k^2} \left[\frac{\gamma^2 + 1}{2} \left(\frac{\omega}{c_s k} \right)^2 + 1 \right] \right. \\ & \left. + \left[\frac{1}{2} (\gamma^2 - 1)^2 h^2 k^2 - 3 \right] \left(\frac{\omega}{c_s k} \right)^2 \right\}, \end{aligned} \quad (\text{B.4})$$

594 which has the property that it consists of two uncoupled modes.

595 The first mode, corresponding to the first curly-bracketed term, is identical to the
596 long wavelength symmetric Lamb wave mode. Its phase velocity is given by Equation 9.

597 The second mode, corresponding to the second curly-bracketed term, is a modifica-
598 tion of the long wavelength antisymmetric Lamb wave mode. The dispersion relation for
599 this mode is,

$$(1 - \gamma^2) h^2 k^2 + \frac{3T}{h\mu k^2} \left[\frac{\gamma^2 + 1}{2} \left(\frac{\omega}{c_s k} \right)^2 + 1 \right] + \left[\frac{1}{2} (\gamma^2 - 1)^2 h^2 k^2 - 3 \right] \left(\frac{\omega}{c_s k} \right)^2 = 0. \quad (\text{B.5})$$

600 Keeping only the lowest order terms in the small parameter kh gives

$$Dk^4 - h\rho\omega^2 = -T, \quad (\text{B.6})$$

601 where $D \equiv \mu(1 - \gamma^2)h^3/3$ is the flexural rigidity, which is equivalent to another commonly
602 used expression, $Eh^3/[12(1 - \nu^2)]$.

603 I have not yet made use of the ice-ocean transfer function. The results in this sec-
604 tion up to this point are therefore valid for any ice-ocean transfer function T . Using the
605 transfer function T from Equation A.22 then gives the dispersion equation of Equation 4.

606 C: Wave particle motions

I calculate particle motions by regrouping the general solution (Equations A.4 and A.5) into symmetric and antisymmetric terms. In order to highlight symmetries about the mid-plane of the ice layer, I define the coordinate $z' \equiv z - h/2$. The ice-atmosphere and ice-ocean surfaces are then located at $z' = \pm h$. These terms correspond to extensional and flexural motions, respectively,

$$\frac{U_x^F}{A} = ik \sin \alpha z' - i \frac{D}{A} \beta \sin \beta z', \quad (\text{C.1})$$

$$\frac{U_z^F}{A} = \alpha \cos \alpha z' + \frac{D}{A} k \cos \beta z', \quad (\text{C.2})$$

$$\frac{U_x^E}{C} = i \frac{B}{C} k \cos \alpha z' + i \beta \cos \beta z', \quad (\text{C.3})$$

$$\frac{U_z^E}{C} = -\frac{B}{C} \alpha \sin \alpha z' + k \sin \beta z'. \quad (\text{C.4})$$

The ratios D/A and B/C are defined from the zero shear stress boundary conditions at $z' = \pm h/2$, as expressed in the second and fourth lines of the matrix in Equation A.25,

$$\frac{B}{C} = \frac{(k^2 - \beta^2) \sin(h\beta/2)}{2k\alpha \sin(h\alpha/2)} \quad (\text{C.5})$$

$$\frac{D}{A} = \frac{2k\alpha \cos(h\alpha/2)}{(\beta^2 - k^2) \cos(h\beta/2)} \quad (\text{C.6})$$

607 The other boundary conditions enter through the requirement that k and ω be related by
608 the dispersion relation. In the long wavelength limit, $B/C \approx D/A \approx -i$. The equations
609 for particle motion (Equations C.1-C.6), combined with the elastic constitutive relation
610 (Equation A.3), suffice to calculate the impedance tensor of Equation 1.

Extensional waves have particle motions,

$$\frac{U_x^E}{C} \approx -2k, \quad (\text{C.7})$$

$$\frac{U_z^E}{C} \approx 2i(kz')k. \quad (\text{C.8})$$

I note that the long wavelength limit $kh \ll 1$ is distinct from the quasi static limit where $\omega/(kc_p) \ll 1$. In other words, long wavelength extensional waves are not quasi static. The long wavelength extensional mode has dominantly horizontal displacements $|U_x^E|/|U_z^E| \sim (kz')^{-1}$ that are constant throughout the ice layer. The much smaller vertical displacements, in contrast, are antisymmetric about the midplane of the ice layer.

Flexural motions have phase velocity given by Equation 4. The particle motions satisfy,

$$\frac{U_x^F}{A} \approx -\frac{k^2 \omega^2 z'}{2\gamma^2} \quad (\text{C.9})$$

$$\frac{U_z^F}{A} \approx -\frac{ik\omega^2}{2\gamma^2} \quad (\text{C.10})$$

Unlike the extensional mode, the flexural mode long wavelength limit is also quasi static. The long wavelength flexural mode has dominantly vertical displacements $|U_z^F|/|U_x^F| \sim (kz)^{-1}$ that are constant throughout the ice layer. The much smaller horizontal displacements, in contrast, are antisymmetric about the midplane of the ice layer.

Acknowledgments

This work was supported by a Postdoctoral Fellowship in the Department of Earth and Planetary Sciences at Harvard University. Discussions with Catherine Walker, Jim Rice, and Doug MacAyeal provided useful context for this study. Greg Wagner read an early version of this paper and provided feedback. Victor Tsai demanded better explanations. Marine Denolle asked several important questions. Olga Sergienko and an anonymous reviewer provided comments that significantly improved the quality of the manuscript. All of the data used in this study have been previously published: the seismic data are freely available at the IRIS Consortium website (http://doi.org/10.7914/SN/XV_2003 and http://doi.org/10.7914/SN/X9_2004) and the satellite imagery is available on the NSIDC website (http://nsidc.org/data/iceshelves_images/index_modis.html). Maps were made using the Antarctic mapping tools for MATLAB [*Greene et al.*, 2017].

References

- Alley, R. B., T. K. Dupont, B. R. Parizek, and S. Anandakrishnan (2005), Access of surface meltwater to beds of sub-freezing glaciers: preliminary insights, *Annals of Glaciology*, 40, 8–14.
- Banwell, A. F., I. C. Willis, G. J. Macdonald, B. Goodsell, D. P. Mayer, A. Powell, and D. R. Macayeal (2017), Calving and rifting on the McMurdo Ice Shelf, Antarctica, *Annals of Glaciology*, pp. 1–10.
- Barenblatt, G. I. (1962), The mathematical theory of equilibrium cracks in brittle fracture, in *Advances in Applied Mechanics*, vol. 7, pp. 55–129, Elsevier.
- Bassis, J. N., R. Coleman, H. Fricker, and J. Minster (2005), Episodic propagation of a rift on the Amery Ice Shelf, East Antarctica, *Geophysical Research Letters*, 32(6).
- Bassis, J. N., H. A. Fricker, R. Coleman, Y. Bock, J. Behrens, D. Darnell, M. Okal, and J.-B. Minster (2007), Seismicity and deformation associated with ice-shelf rift propagation, *Journal of Glaciology*, 53(183), 523–536.
- Bassis, J. N., H. A. Fricker, R. Coleman, and J.-B. Minster (2008), An investigation into the forces that drive ice-shelf rift propagation on the Amery Ice Shelf, East Antarctica, *Journal of Glaciology*, 54(184), 17–27.
- Bažant, Z. P. (1992), Large-scale thermal bending fracture of sea ice plates, *Journal of Geophysical Research: Oceans*, 97(C11), 17,739–17,751.
- Bažant, Z. P. (1993), Scaling laws in mechanics of failure, *Journal of Engineering Mechanics*, 119(9), 1828–1844.

- 653 Benn, D. I., C. R. Warren, and R. H. Mottram (2007), Calving processes and the dynam-
654 ics of calving glaciers, *Earth-Science Reviews*, 82(3), 143–179.
- 655 Borstad, C., A. Khazendar, E. Larour, M. Morlighem, E. Rignot, M. Schodlok, and
656 H. Seroussi (2012), A damage mechanics assessment of the Larsen B ice shelf prior to
657 collapse: Toward a physically-based calving law, *Geophysical Research Letters*, 39(18).
- 658 Borstad, C., E. Rignot, J. Mouginot, and M. Schodlok (2013), Creep deformation and but-
659 tressing capacity of damaged ice shelves: theory and application to Larsen C ice shelf,
660 *The Cryosphere*, 7(6).
- 661 Borstad, C., D. McGrath, and A. Pope (2017), Fracture propagation and stability of ice
662 shelves governed by ice shelf heterogeneity, *Geophysical Research Letters*, 44(9), 4186–
663 4194.
- 664 Broek, D. (2012), *Elementary engineering fracture mechanics*, Springer Science & Busi-
665 ness Media.
- 666 Bromirski, P., Z. Chen, R. Stephen, P. Gerstoft, D. Arcas, A. Diez, R. Aster, D. Wiens,
667 and A. Nyblade (2017), Tsunami and infragravity waves impacting Antarctic ice
668 shelves, *Journal of Geophysical Research: Oceans*.
- 669 Bromirski, P. D., O. V. Sergienko, and D. R. MacAyeal (2010), Transoceanic infragravity
670 waves impacting Antarctic ice shelves, *Geophysical Research Letters*, 37(2).
- 671 Bromirski, P. D., A. Diez, P. Gerstoft, R. A. Stephen, T. Bolmer, D. A. Wiens, R. C.
672 Aster, and A. Nyblade (2015), Ross ice shelf vibrations, *Geophysical Research Letters*,
673 42(18), 7589–7597.
- 674 Brunt, K. M., E. A. Okal, and D. R. MacAyeal (2011), Antarctic ice-shelf calving trig-
675 gered by the Honshu (Japan) earthquake and tsunami, March 2011, *Journal of Glaciol-
676 ogy*, 57(205), 785–788.
- 677 Cathles, L., E. A. Okal, and D. R. MacAyeal (2009), Seismic observations of sea swell on
678 the floating Ross Ice Shelf, Antarctica, *Journal of Geophysical Research: Earth Surface*,
679 114(F2).
- 680 DeFranco, S. J., and J. P. Dempsey (1994), Crack propagation and fracture resistance in
681 saline ice, *Journal of Glaciology*, 40(136), 451–462.
- 682 Doake, C., H. Corr, H. Rott, P. Skvarca, and N. Young (1998), Breakup and conditions for
683 stability of the northern Larsen Ice Shelf, Antarctica, *Nature*, 391(6669), 778–780.
- 684 Duddu, R., and H. Waisman (2013), A nonlocal continuum damage mechanics approach to
685 simulation of creep fracture in ice sheets, *Computational Mechanics*, pp. 1–14.
- 686 Duddu, R., J. Bassis, and H. Waisman (2013), A numerical investigation of surface
687 crevasse propagation in glaciers using nonlocal continuum damage mechanics, *Geo-
688 physical Research Letters*, 40(12), 3064–3068.
- 689 Dugdale, D. S. (1960), Yielding of steel sheets containing slits, *Journal of the Mechanics
690 and Physics of Solids*, 8(2), 100–104.
- 691 Fretwell, P., H. D. Pritchard, D. G. Vaughan, J. Bamber, N. Barrand, R. Bell, C. Bianchi,
692 R. Bingham, D. Blankenship, G. Casassa, et al. (2013), Bedmap2: improved ice bed,
693 surface and thickness datasets for antarctica, *The Cryosphere*.
- 694 Freund, L. (1972a), Crack propagation in an elastic solid subjected to general loading i.
695 constant rate of extension, *Journal of the Mechanics and Physics of Solids*, 20(3), 129–
696 140.
- 697 Freund, L. (1972b), Crack propagation in an elastic solid subjected to general loading ii.
698 non-uniform rate of extension, *Journal of the Mechanics and Physics of Solids*, 20(3),
699 141–152.
- 700 Freund, L. B. (1998), *Dynamic fracture mechanics*, Cambridge university press.
- 701 Fricker, H., N. Young, R. Coleman, J. Bassis, and J.-B. Minster (2005), Multi-year mon-
702 itoring of rift propagation on the Amery Ice Shelf, East Antarctica, *Geophysical Re-
703 search Letters*, 32(2).
- 704 Gill, A. E. (2016), *Atmosphere and ocean dynamics*, Elsevier.
- 705 Graff, K. F. (2012), *Wave motion in elastic solids*, Courier Corporation.

- 706 Greene, C. A., D. E. Gwyther, and D. D. Blankenship (2017), Antarctic mapping tools for
707 MATLAB, *Computers and Geosciences*, 104, 151–157.
- 708 Greenhill, A.-G. (1886), Wave motion in hydrodynamics, *American Journal of Mathemat-*
709 *ics*, pp. 62–96.
- 710 Griffith, A. A. (1921), The phenomena of rupture and flow in solids, *Philosophical trans-*
711 *actions of the royal society of london. Series A, containing papers of a mathematical or*
712 *physical character*, 221, 163–198.
- 713 Holdsworth, G. (1969), Flexure of a floating ice tongue, *Journal of Glaciology*, 8(54),
714 385–397.
- 715 Holdsworth, G., and J. Glynn (1978), Iceberg calving from floating glaciers by a vibrating
716 mechanism, *Nature*, 274(5670), 464–466.
- 717 Holland, P. R., H. F. Corr, D. G. Vaughan, A. Jenkins, and P. Skvarca (2009), Marine ice
718 in Larsen ice shelf, *Geophysical Research Letters*, 36(11).
- 719 Hulbe, C. L., C. LeDOUX, and K. Cruikshank (2010), Propagation of long fractures in
720 the Ronne Ice Shelf, antarctica, investigated using a numerical model of fracture propa-
721 gation, *Journal of Glaciology*, 56(197), 459–472.
- 722 Irwin, G. R. (1957), Analysis of stresses and strains near the end of a crack traversing a
723 plate, *Journal of applied mechanics*, 24(3), 361–364.
- 724 Jacobs, S., D. MacAyeal, and J. Ardai (1986), The recent advance of the Ross Ice Shelf
725 Antarctica, *Journal of Glaciology*, 32(112), 464–474.
- 726 Jansen, D., A. Luckman, B. Kulesa, P. R. Holland, and E. C. King (2013), Marine ice
727 formation in a suture zone on the Larsen C Ice Shelf and its influence on ice shelf dy-
728 namics, *Journal of Geophysical Research: Earth Surface*, 118(3), 1628–1640.
- 729 Joughin, I., and D. R. MacAyeal (2005), Calving of large tabular icebergs from ice shelf
730 rift systems, *Geophysical research letters*, 32(2).
- 731 Keys, H. J., S. S. Jacobs, and L. W. Brigham (1998), Continued northward expansion of
732 the Ross Ice Shelf, Antarctica, *Annals of Glaciology*, 27, 93–98.
- 733 Kononov, Y. (2014), Ice-shelf resonance deflections modelled with a 2-D elastic centre-
734 line model, *Phys. Rev. Res. Int*, 4, 9–29.
- 735 Krawczynski, M. J., M. D. Behn, S. B. Das, and I. Joughin (2009), Constraints on the lake
736 volume required for hydro-fracture through ice sheets, *Geophysical Research Letters*,
737 36(10).
- 738 Krug, J., J. Weiss, O. Gagliardini, and G. Durand (2014), Combining damage and fracture
739 mechanics to model calving, *The Cryosphere Discussions*, 8(1), 1111–1150.
- 740 Larour, E., E. Rignot, and D. Aubry (2004a), Processes involved in the propagation of
741 rifts near Hemmen ice rise, Ronne ice shelf, Antarctica, *Journal of Glaciology*, 50(170),
742 329–341.
- 743 Larour, E., E. Rignot, and D. Aubry (2004b), Modelling of rift propagation on Ronne Ice
744 Shelf, Antarctica, and sensitivity to climate change, *Geophysical research letters*, 31(16).
- 745 LeDoux, C. M., C. L. Hulbe, M. P. Forbes, T. A. Scambos, and K. Alley (2017), Struc-
746 tural provinces of the Ross Ice Shelf, Antarctica, *Annals of Glaciology*, pp. 1–11.
- 747 Lemaitre, J. (1985), A continuous damage mechanics model for ductile fracture, *Transac-*
748 *tions of the ASME. Journal of Engineering Materials and Technology*, 107(1), 83–89.
- 749 Lipovsky, B. P., and E. M. Dunham (2015), Vibrational modes of hydraulic fractures: In-
750 ference of fracture geometry from resonant frequencies and attenuation, *Journal of Geo-*
751 *physical Research: Solid Earth*, 120(2), 1080–1107.
- 752 Lipovsky, B. P., and E. M. Dunham (2016), Tremor during ice-stream stick slip, *The*
753 *Cryosphere*, 10(1), 385–399.
- 754 Lipovsky, B. P., and E. M. Dunham (2017), Slow-slip events on the Whillans Ice Plain,
755 Antarctica, described using rate-and-state friction as an ice stream sliding law, *Journal*
756 *of Geophysical Research: Earth Surface*, 122(4), 973–1003.
- 757 MacAyeal, D. R., E. Rignot, and C. L. Hulbe (1998), Ice-shelf dynamics near the
758 front of the Filchner-Ronne Ice Shelf, Antarctica, revealed by sar interferometry:
759 model/interferogram comparison, *Journal of Glaciology*, 44(147), 419–428.

- 760 MacAyeal, D. R., E. A. Okal, R. C. Aster, J. N. Bassis, K. M. Brunt, L. M. Cathles,
761 R. Drucker, H. A. Fricker, Y.-J. Kim, S. Martin, et al. (2006), Transoceanic wave prop-
762 agation links iceberg calving margins of Antarctica with storms in tropics and Northern
763 Hemisphere, *Geophysical Research Letters*, 33(17).
- 764 Malvern, L. E. (1969), *Introduction to the Mechanics of a Continuous Medium*, Monograph,
765 Pearson.
- 766 McGrath, D., K. Steffen, H. Rajaram, T. Scambos, W. Abdalati, and E. Rignot (2012),
767 Basal crevasses on the Larsen C Ice Shelf, Antarctica: Implications for meltwater pond-
768 ing and hydrofracture, *Geophysical Research Letters*, 39(16).
- 769 McGrath, D., K. Steffen, P. R. Holland, T. Scambos, H. Rajaram, W. Abdalati, and E. Rignot
770 (2014), The structure and effect of suture zones in the Larsen C Ice Shelf, Antarc-
771 tica, *Journal of Geophysical Research: Earth Surface*, 119(3), 588–602.
- 772 Munk, W. H., G. Miller, F. Snodgrass, and N. Barber (1963), Directional recording of
773 swell from distant storms, *Philosophical Transactions of the Royal Society of London*.
774 A, 255(1062), 505–584.
- 775 Nemat-Nasser, S., A. Oranratnachai, and L. Keer (1979), Spacing of water-free crevasses,
776 *Journal of Geophysical Research: Solid Earth*, 84(B9), 4611–4620.
- 777 Plate, C., R. Müller, A. Humbert, and D. Gross (2012), Evaluation of the criticality of
778 cracks in ice shelves using finite element simulations, *The Cryosphere*, 6(5), 973.
- 779 Powell, A. (2015), Frozen South: Ice Breakout, <https://vimeo.com/159039693>.
- 780 Pralong, A., and M. Funk (2005), Dynamic damage model of crevasse opening and appli-
781 cation to glacier calving, *Journal of Geophysical Research: Solid Earth*, 110(B1).
- 782 Press, F., and M. Ewing (1951), Propagation of elastic waves in a floating ice sheet, *Eos*,
783 *Transactions American Geophysical Union*, 32(5), 673–678.
- 784 Reeh, N. (1968), On the calving of ice from floating glaciers and ice shelves, *Journal of*
785 *Glaciology*, 7(50), 215–232.
- 786 Rice, J. R. (1968), A path independent integral and the approximate analysis of strain con-
787 centration by notches and cracks, *Journal of applied mechanics*, 35(2), 379–386.
- 788 Rice, J. R. (2001), New perspectives on crack and fault dynamics, in *Mechanics for a New*
789 *Millennium*, pp. 1–24, Springer.
- 790 Rice, J. R., and N. Levy (1972), The part-through surface crack in an elastic plate, *Jour-*
791 *nal of Applied Mechanics*, 39(1), 185–194.
- 792 Rice, J. R., and D. M. Tracey (1969), On the ductile enlargement of voids in triaxial stress
793 fields, *Journal of the Mechanics and Physics of Solids*, 17(3), 201–217.
- 794 Rignot, E., and D. R. MacAyeal (1998), Ice-shelf dynamics near the front of the Filchner
795 Ronne Ice Shelf, Antarctica, revealed by SAR interferometry, *Journal of Glaciology*,
796 44(147), 405–418.
- 797 Rignot, E., G. Casassa, P. Gogineni, W. Krabill, A. Rivera, and R. Thomas (2004), Accel-
798 erated ice discharge from the Antarctic Peninsula following the collapse of Larsen B ice
799 shelf, *Geophysical Research Letters*, 31(18).
- 800 Rist, M., P. Sammonds, H. Oerter, and C. Doake (2002), Fracture of Antarctic shelf ice,
801 *Journal of Geophysical Research: Solid Earth*, 107(B1).
- 802 Robin, G. d. Q. (1979), Formation, flow, and disintegration of ice shelves, *Journal of*
803 *Glaciology*, 24(90), 259–271.
- 804 Scambos, T., T. Haran, M. Fahnestock, T. Painter, and J. Bohlander (2007), MODIS-based
805 mosaic of Antarctica (MOA) data sets: Continent-wide surface morphology and snow
806 grain size, *Remote Sensing of Environment*, 111(2-3), 242–257.
- 807 Scambos, T., H. A. Fricker, C.-C. Liu, J. Bohlander, J. Fastook, A. Sargent, R. Massom,
808 and A.-M. Wu (2009a), Ice shelf disintegration by plate bending and hydro-fracture:
809 Satellite observations and model results of the 2008 Wilkins Ice Shelf break-ups, *Earth*
810 *and Planetary Science Letters*, 280(1), 51–60.
- 811 Scambos, T., J. Bohlander, and B. Raup (2009b), Images of Antarctic ice shelves, *National*
812 *Snow and Ice Data Center*, online available at: <http://nsidc.org/data/iceshelves/images>.

- 813 Scambos, T. A., J. Bohlander, C. u. Shuman, and P. Skvarca (2004), Glacier acceleration
814 and thinning after ice shelf collapse in the Larsen B embayment, Antarctica, *Geophysical*
815 *Research Letters*, 31(18).
- 816 Schulson, E. M., P. Duval, et al. (2009), *Creep and fracture of ice*, vol. 1, Cambridge Uni-
817 versity Press Cambridge.
- 818 Sergienko, O. (2010), Elastic response of floating glacier ice to impact of long-period
819 ocean waves, *Journal of Geophysical Research: Earth Surface*, 115(F4).
- 820 Sergienko, O. (2013), Normal modes of a coupled ice-shelf/sub-ice-shelf cavity system,
821 *Journal of Glaciology*, 59(213), 76–80.
- 822 Sergienko, O. (2017), Behavior of flexural gravity waves on ice shelves: Application to the
823 Ross Ice Shelf, *Journal of Geophysical Research: Oceans*.
- 824 Shabtaie, S., and C. R. Bentley (1982), Tabular icebergs: implications from geophysical
825 studies of ice shelves, *Journal of Glaciology*, 28(100), 413–430.
- 826 Sih, G. C. (2012), *Plates and shells with cracks: a collection of stress intensity factor solu-*
827 *tions for cracks in plates and shells*, vol. 3, Springer Science & Business Media.
- 828 Smith, R. (1976), The application of fracture mechanics to the problem of crevasse pene-
829 tration, *Journal of Glaciology*, 17(76), 223–228.
- 830 Van der Veen, C. (1998), Fracture mechanics approach to penetration of surface crevasses
831 on glaciers, *Cold Regions Science and Technology*, 27(1), 31–47.
- 832 Vaughan, D. G. (1995), Tidal flexure at ice shelf margins, *Journal of Geophysical Re-*
833 *search: Solid Earth*, 100(B4), 6213–6224.
- 834 Walker, C., J. Bassis, H. Fricker, and R. Czerwinski (2013), Structural and environmental
835 controls on Antarctic ice shelf rift propagation inferred from satellite monitoring, *Jour-*
836 *nal of Geophysical Research: Earth Surface*, 118(4), 2354–2364.
- 837 Walker, C. C., J. N. Bassis, H. A. Fricker, and R. J. Czerwinski (2015), Observations of
838 interannual and spatial variability in rift propagation in the Amery Ice Shelf, Antarctica,
839 2002–14, *Journal of Glaciology*, 61(226), 243–252.
- 840 Wang, R., and H. H. Shen (2010), Gravity waves propagating into an ice-covered ocean:
841 A viscoelastic model, *Journal of Geophysical Research: Oceans*, 115(C6).
- 842 Weertman, J. (1957), Deformation of floating ice shelves, *Journal of glaciology*, 3(21), 38–
843 42.
- 844 Weertman, J. (1971), Theory of water-filled crevasses in glaciers applied to vertical
845 magma transport beneath oceanic ridges, *Journal of Geophysical Research*, 76(5), 1171–
846 1183.
- 847 Weertman, J. (1973), Can a water-filled crevasse reach the bottom surface of a glacier,
848 *IASH publ*, 95, 139–145.
- 849 Weiss, J. (2004), Subcritical crack propagation as a mechanism of crevasse formation and
850 iceberg calving, *Journal of Glaciology*, 50(168), 109–115.
- 851 Williams, R., and E. Robinson (1981), Flexural waves in the Ross Ice Shelf, *Journal of*
852 *Geophysical Research: Oceans*, 86(C7), 6643–6648.
- 853 Yu, H., E. Rignot, M. Morlighem, and H. Seroussi (2017), Iceberg calving of Thwaites
854 Glacier, West Antarctica: full-Stokes modeling combined with linear elastic fracture
855 mechanics, *The Cryosphere*, 11(3), 1283–1296, doi:10.5194/tc-11-1283-2017.